Energy Conversion and Management 250 (2021) 114884

Contents lists available at ScienceDirect

Energy Conversion and Management

journal homepage: www.elsevier.com/locate/enconman

In-pipe axial pico-hydraulic tailored turbine design: A novel approach using a dimensionless design chart

Abraham Vivas [a], A. Viedma [a,*], A. S. Kaiser [a]

[a] Dep. Ing. Térmica y de Fluidos, Universidad Politécnica de Cartagena, Dr. Fleming, s/n, 30202 Cartagena, Spain

ARTICLE INFO

Keywords:
Turbomachinery design
Bi-dimensional cascade theory
Energy efficiency
Computational fluid dynamics
OpenFOAM

ABSTRACT

Energy consumed by the water industry is not negligible and improvements on energy efficiency in water distribution networks are still needed. This work aims to provide a new approach to design tailored torpedo shaped in-pipe axial pico-hydraulic turbines for the recovery of energy in water distribution networks. Simple straight untwisted blades with arc of circles profiles are imposed to simplify manufacturing. Ideal flow bi-dimensional cascade theory with Weinel isolated airfoil to cascade correlations are used as compromise between accuracy and simplicity. From it, a dimensionless design chart is build. A novel flow-to-head factor is chosen as main dimensionless factor to simplify stator analysis and obtain a more compact chart. From five usual input design parameters, choosing the value of three, and letting two of them to vary allows the trace of a space of all optimal designs. From this space, a turbine or family of turbines can be obtained. A design example on the same conditions as a experimentally tested turbine found in the literature was carried over and simulated with OpenFOAM open source library. A mesh parametric study for numerical validation purposes is realized. Discretization uncertainty found for the selected mesh was about one point for the hydraulic efficiency. The designed and simulated turbine showed a maximum hydraulic efficiency of 65%. The presented non-dimensional approach proved to be useful to design efficient tailored simple pico-hydraulic turbines for energy recovery in distribution water networks, relaying on one design chart.

1. Introduction

Hydraulic energy is a mature and reliable technology that generates renewable energy world wide [1,2], nevertheless for pico-hydraulic schemes innovation on improvements and affordability are still needed [3]. Micro and pico power range are usually defined as the ones not exceeding 100 kW and 5 kW respectively [3].

Energy consumption on water industry represents up to 3% of the world's total consumption, and from this up to 45% is due to processes on water distribution networks (WDN) [4,5]. Some studies show that surplus pressure head on WDN can be recovered and represents a feasible alternative to improve energy efficiency [5,6]. For this reason, in recent years, many attempts have been made to develop cheap turbines or to improve the selection and operation of pumps working as turbines (PaTs) to recover pico-hydraulic energy in WDN.

Usually PaTs studies are focused on surpassing the main barrier to its adoption: the characterization of the hydraulic behavior and the improvement of operation within the network [7–9].

Some of the most relevant pico-hydraulic turbine developments for the recovery of energy on WDN include:

- The five blade tubular propeller (5BTP): a single propeller, based on the assumptions of free vortex radial velocity distribution and perfect guidance of the flow, featuring arc of circles as profiles for lowering the cost of manufacturing [10,11].
- The Duo-Turbo project: a compact tubular design with two counter rotating rotors. This project applies Euler's turbine equation, velocity triangles and perfect guidance of the flow as design method. It features modified NACA airfoils for the blades [12,13].
- A cross-flow turbine: based on the design of a flow blocking geometry and the perfect guidance hypothesis on the maximum cross-section of the turbine. Heavily guided by experiments and numerical simulations, it features arc of circle profiles for the blades [14,15].

Other developments include a drag-based vertical axis design [16,17], a spherical Darrieus-like cross flow turbine [18] and a vertical axis simple device branded as "GreenValve" [19].

All the previous designs have in common that they are not that simple of manufacture (having twisted blades or complicated airfoils)

* Corresponding author.
E-mail address: abraham.vivasb@edu.upct.es (A. Vivas).

https://doi.org/10.1016/j.enconman.2021.114884
Received 2 May 2021; Received in revised form 11 October 2021; Accepted 13 October 2021
Available online 9 November 2021

Nomenclature

Latin Letters

ar	Blade aspect ratio
C	Absolute speed
C_D	Drag coeffficient
C_L	Lift coefficient
C_{L0}	Lift coefficient at zero angle of attack of the isolated airfoil
ΔC	Change in speed
D	Diameter
F_n, G_n	General function symbols, where n is a natural number
f	Flow-to-head factor
f_A	Area factor
F_L	Lift force
gdc	Greatest common divisor
g	Gravitational acceleration constant
H	Hydraulic head or head pressure drop
h	Airfoil camber
I	Turbulence intensity
L	Axial dimension of an element of the turbine
l	Chord length
$\dot{m}$	Mass flow rate
N	Number of cell elements
n	Angular speed in revolutions per minute
Re	Reynolds number
R	A particular radial station
thk	Airfoil thickness
T	Hub-to-tip ratio
t	Spacing or pitch
U	Tangential speed
$\dot{W}$	Mechanical power on the shaft
W	Relative speed
xtr	Distance from the leading edge to the laminar-turbulent transition point
X_1, X_2	General variables that represent the soft constraints
y^+	Dimensionless wall distance to the first element of the mesh in the boundary layer
Z	Number of blades

Greek Letters

α	Absolute velocity flow angle
α_{AOA}	Angle of attack
β	Relative velocity flow angle
ϵ	Maximum relative error between cylindrical and flat projection
ϕ	Flow factor
γ	Stagger angle
η_h	Hydraulic efficiency
μ_0, μ_1, μ_2	Weinel relation coefficients
ν	Kinematic viscosity
Ω_s	Specific speed
ψ	Head factor
ρ	Density of the fluid
σ	Cascade solidity
τ	Mechanical torque on the shaft
ω	Angular speed in radians per second

Subscripts

1	General cascade or stage upstream variable
2	General cascade or interstage variable
3	Stage downstream variable
3D	Relative to a variable that takes in account the three dimensional effects on the turbine
a	Relative to the axial direction
BEP	Relative to the best efficiency point
db	Relative to the downstream bulb
flw	Relative to the flow pattern on the bi-dimensional cascades
geo	Relative to the geometry of the blade cascades
h	Relative to the hub
m	Relative to the mean
opt	Relative to the optimal operation point
p	Relative to the pipe
R	Relative to the rotor
S	Relative to the stator
θ	Relative to the tangential direction
ub	Relative to the upstream bulb
u	Relative to the “useful” energy (hydraulic energy trasnferred to the shaft)

or, in some cases, have poor performance. In addition, their design process is based on perfectly guided flow (ignoring the bi-dimensional cascade theory) or depends greatly on fluid simulation and experimentation. Another feature that lacks in the mentioned developments is a compact generalized method.

An observation that can be made is that axial tubular turbine configurations usually display better performance than its cross-flow counterparts, recovering energy from small pressure drops on high flow rate sections of the water network.

In the consulted bibliography of design of axial turbomachinery, authors like Lewis [20] and Dixon [21] describes the theory of bi-dimensional cascades in the context of thermal turbomachinery design. They deduce the equations of global balances on cascades and turbine stages in dimensionless form, most of them applicable to hydraulic turbines, given the fact that the base hypothesis is incompressible flow. Both authors heavily focus on correlations obtained from experiments to relate energy losses to velocity triangle parameters (like inlet/outlet flow angles or flow, head and reaction factors). Both author’s design logic is to find the most efficient turbine stage velocity triangle parameters, number of blades and space-chord ratio from the many criteria, experimental correlations and charts described by them. To complete the design, by defining the shape of the blades, Dixon [21] recommends the use of numerical simulations, while Lewis [20] directly applies a companion software that calculates the ideal flow for bi-dimensional cascades.

Other authors like Rey et al. [22,23] and Mataix and Alonso [24] directly apply the bi-dimensional cascade theory to the design of hydraulic turbomachinery. Rey et al. [22,23] focus on the flow angles as their main dimensionless parameters. They develop correlations from experimental tests done by NACA on compression cascades [25] to predict the blade cascade geometry performance. Rey et al. [22,23] developments are made in the context of pump design, concluding with dimensionless design charts based on the mean flow angles for stator and rotor cascades of the pump stages. Mataix and Alonso [24] shows a dimensional procedure to design propeller turbomachinery. They apply the Weinig [26] and Weinel [27] correlations to relate the performance of isolated airfoils to the performance of bi-dimensional cascades. To complement the lack of energy loss information, Mataix and Alonso [24]

propose its own criterion to choose the lift coefficient of the cascade given the performance of the isolated airfoil. They estimate global efficiencies and apply this methodology to a pump design.

This work aims to develop, describe and apply a tubular turbine design method that address some of the features and characteristics that lacks in previous studies, in particular:

- To remove the perfect guidance hypothesis using the bi-dimensional cascade theory.
- To produce dimensionless design charts that directly relate the design flow variables with the geometric and operational characteristics of the desired family of turbines.
- To make the design charts compact by the introduction of a novel flow-to-head factor.
- To achieve the best compromise between simplicity and accuracy, using the isolated-to-cascade correlations given that there are widely available data on isolated airfoil's performance.
- To reduce manufacture complexity by limiting the design to straight untwisted blades and the usage of arc of circles as blade profiles.
- To propose bulb geometric proportions to complete the layout.

This work was inspired by Rey et al. [22,23] dimensionless charts, follows the isolated-to-cascade philosophy showed by Mataix and Alonso [24] and use flow and head factors widely implemented by Lewis [20] and Dixon [21], adding the authors own insights.

A design example on the same conditions as an experimentally tested turbine is carried over. A numerical validation parametric study is developed and from the resulting parameters the design example is numerically simulated. The obtained off-design performance curves are compared against the tested reference turbine.

2. Dimensionless design method

2.1. Geometry overview

This method allows the design of axial in-pipe hydraulic turbines. In Fig. 1 the general morphology of such turbines is shown. It is composed by an upstream rounded bulb, an axial stator-rotor stage and a downstream bulb that allows an efficient pressure recovery. The turbine stage is composed by simple, constant length, untwisted blades to simplify manufacturing. Even though any airfoil shape could be used, on this work arc of circles are chosen as the shape of the blade profiles. This shape is chosen because is the second most simple after the flat plate, allowing for improved aerodynamic performance without introducing significant geometrical complexity.

In Fig. 2 the proposed internal elements of the turbine are shown. The upstream bulb-stator block is proposed to be fixed to the pipe, while the downstream bulb could contain the electric generator and be supported by straight blades. It can be noticed that the wiring can be conducted through one of the supports.

Taking care that radial component of the flow velocities on the stator-rotor stage remains small, the flow can be studied on the bi-dimensional unwrapped surfaces of cylindrical cuts as shown in Fig. 3. This kind of study leads to the bi-dimensional cascade theory, where the stator-rotor stage can be decomposed into infinite bi-dimensional blade cascades. Given the geometric simplicity proposed for the blades in this work, the minimum information needed to describe the geometry and approximate the flow can be obtained from the study of the mean radius cutting surface.

The geometry of a general blade cascade can be described as shown in Fig. 4. It includes the stagger angle γ, the chord length l and the spacing or pitch t. The complete dimensionless description of a blade

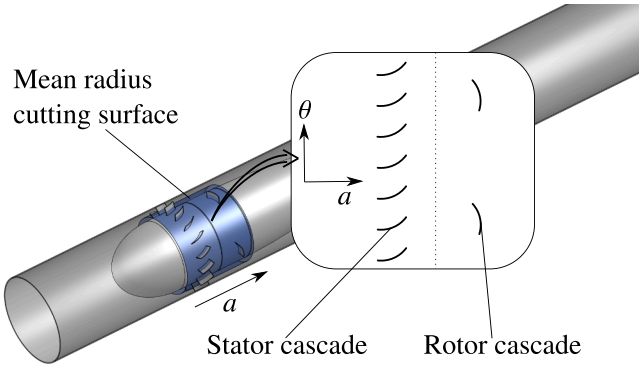

Fig. 1. Morphology and elements of turbines that can be designed.

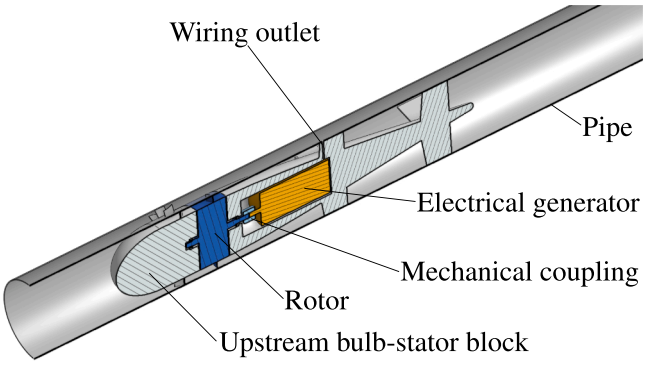

Fig. 2. Section with proposed internal elements of the turbine.

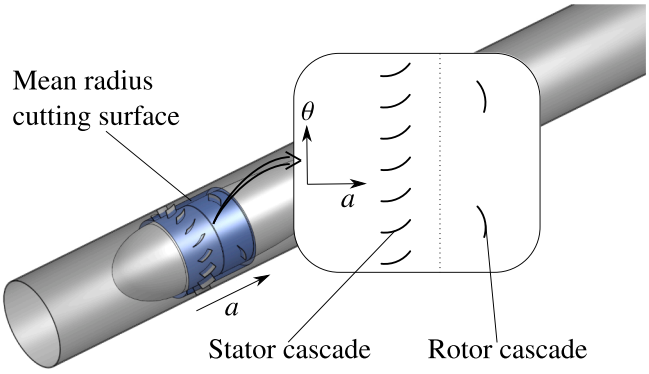

Fig. 3. Detail of the stator-rotor stage bi-dimensional analysis on a cylindrical cut.

cascades can be defined only by two parameters: the stagger angle γ and the solidity σ as defined in Eq. 1.

$$\sigma = \frac{l}{t} = \frac{Zl}{2\pi R} \tag{1}$$

The geometry of the blades can be obtained extruding the airfoil profiles from the unwrapped bi-dimensional cascades. This leads to a very small distortion that will be commented later.

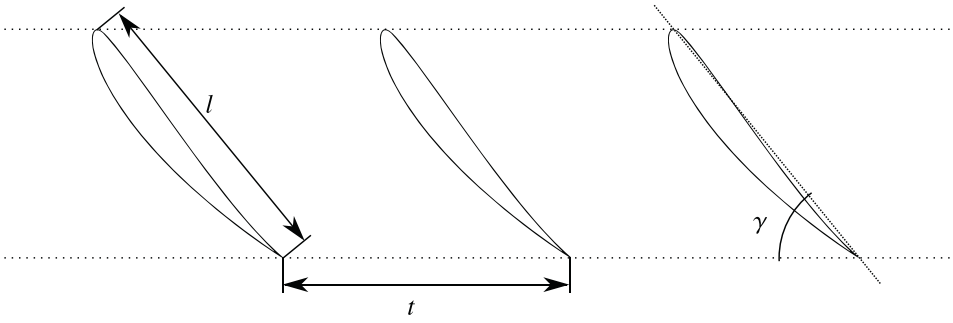

Fig. 4. Cascade geometry parameters.

2.2. Algorithm overview

The method's theoretical base assumptions are the following:

- Bi-dimensional cascade analysis with ideal flow.
- No swirl at stator inlet[1] nor at rotor outlet.
- Mean radius analysis, where the mean radius is given by the Eq. 2.
- Small deviation from radial equilibrium hypothesis, i.e $f_A \geqslant 2$ given the Eq. 3. This condition can be translated in terms of the hub-to-tip ratio using the Eq. 4, obtaining $T \gtrapprox 0.71$.

$$R_m = \frac{R_p + R_h}{2} \tag{2}$$

$$f_A = \frac{A_p}{A_{\text{passage}}} = \frac{R_p^2}{R_p^2 - R_h^2} \tag{3}$$

$$T = \frac{R_h}{R_p} = \sqrt{1 - 1/f_A} \tag{4}$$

Consulted authors in the bibliography deduce the equations for the resulting dimensionless force on the cascades as function of flow angles [20–22]. In this work, the dimensionless force is deduced as function of the chosen dimensionless factors, allowing for a more direct relation between the design constraints and the resulting geometrical variables. The chosen dimensionless factors are the useful head factor ψ_u in Eq. 5 and the novel flow-to-head factor f in Eq. 6, which in turn is function of the flow factor ϕ in Eq. 7. The flow-to-head factor is chosen because it allows further simplification on the analysis of the stator cascade equations. The definition of the tangential speed U is given in Eq. 8. The axial flow velocity on the turbine passage C_a can be expressed in terms of the flow rate Q as shown in Eq. 9.

$$\psi_u = \frac{gH_u}{U^2} \tag{5}$$

$$f = \frac{\phi}{\psi_u} \tag{6}$$

$$\phi = \frac{C_a}{U} \tag{7}$$

$$U = \omega R \tag{8}$$

$$C_a = \frac{Q}{\pi\left(R_p^2 - R_h^2\right)} \tag{9}$$

The algorithm of the design method is summarized on the flow chart shown in Fig. 5. Starting with five dimensional input design parameters, two are chosen to vary on a range to improve the final turbine selection.

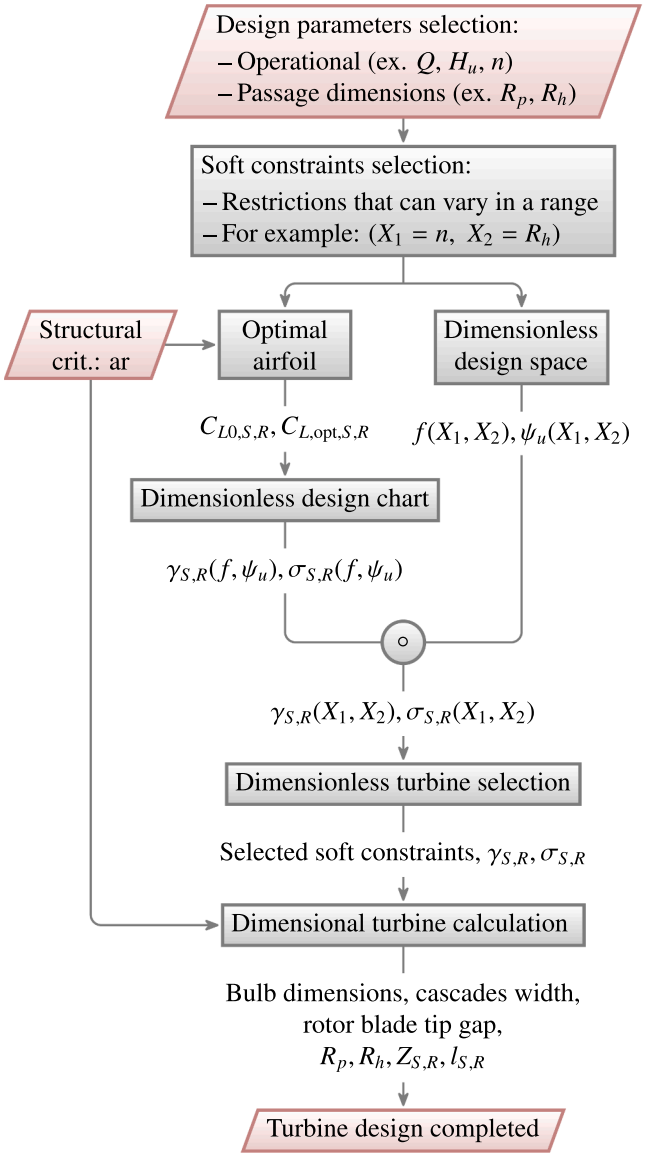

Fig. 5. Flow chart of the algorithm.

From that dimensional parameters, the dimensionless parameters of choice (f,ψ_u) can be calculated. Given that two of them vary, the derived dimensionless parameters describe a set of curves on a two-dimensional dimensionless design space. Choosing the structural input criteria for the blades (aspect ratio ar), the minimum information of the optimal airfoils working at its optimal aerodynamic point can be obtained (lift

[1] On industrial cases where significant inlet swirl is present, an upstream flow rectifier is recommended.

coefficients $C_{L0}, C_{L,\text{opt}}$) for each cascade; from them, the dimensionless design chart can be calculated and built. Combining the design space curves with the dimensionless design chart, the curves that directly relates the design parameters with the geometry of the optimal dimensionless cascades can be obtained. From the curves on the chart, a turbine that improves the off design characteristics is chosen. Finally, adding the aspect ratio (ar) structural criterion, all the dimensional characteristics of the blade rows and bulb can be calculated, obtaining the desired turbine.

Given that the dimensionless design chart contains the core theory of the method, it is explained first followed by the algorithm. Reference cascade width and bulb proportions are given on the design example. The downstream bulb supports and its effects are not studied on this work.

2.3. Dimensionless design chart theory

From now on, all the variables that depends on a general radial station (like the solidity or the dimensionless factors) are assumed to be referring to the mean radius unless otherwise specified.

On ideal flow, the lift coefficient given by the flow pattern corresponds to the dimensionless force on the blade cascade. A complete deduction of stator and rotor flow lift coefficient as function of the dimensionless factors of choice is shown in the appendix A, resulting in Eqs. 10 and 11 respectively.

$$C_{L,\text{flw},S} = \frac{2}{\sigma_S}\left(\frac{1}{\sqrt{f^2+\frac{1}{4}}}\right) \tag{10}$$

$$C_{L,\text{flw},R} = \frac{2}{\sigma_R}\left(\frac{1}{\sqrt{f^2+\left(\frac{1}{\psi_u}-\frac{1}{2}\right)^2}}\right) \tag{11}$$

From Fig. A.25 mean flow angles can be related to the dimensionless factors of choice as shown in the Eqs. 12 and 13.

$$\alpha_m = \arctan(2f) \tag{12}$$

$$\beta_m = \arctan\left(\frac{f}{\frac{1}{\psi_u}-\frac{1}{2}}\right) \tag{13}$$

Lift coefficient can also be obtained from the cascade geometry. To model the geometrical lift coefficients, an isolated-to-cascade relation is used to leverage the widely available data on performance of isolated airfoils. The bibliography shows that Weinel relation is the best compromise between theoretical depth and experimentation for general airfoil shapes [24,27]. The Weinel relation is based on the Eq. 14, where its coefficients can be obtained from Fig. 6–8. The coefficients are only function of the solidity σ and stagger angle γ.

$$C_{L,\text{geo}} = \mu_0 C_{L0}\left(\frac{1-\mu_1 C_{L0}\tan(\gamma)}{1+\mu_1 C_{L0}\tan(\gamma)}\right) + 2\pi\mu_2\sin(\alpha_{AOA}) \tag{14}$$

The angle of attack α_{AOA} on Eq. 14 can be related with the mean flow angle and the stagger angle as shown in Fig. 9, resulting in Eqs. 15 and 16 for the stator and rotor respectively.

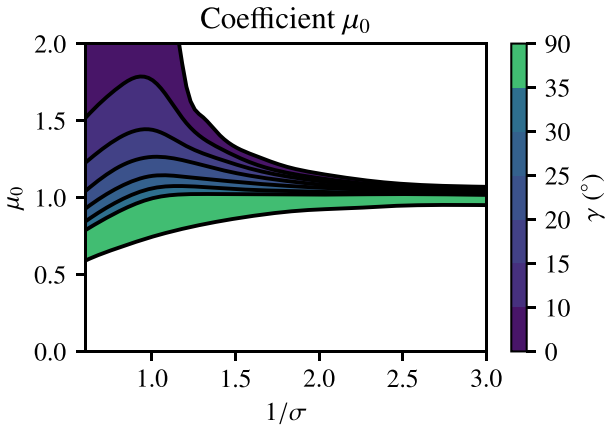

Fig. 6. Contours of interpolated Weinel relation coefficient μ_0.

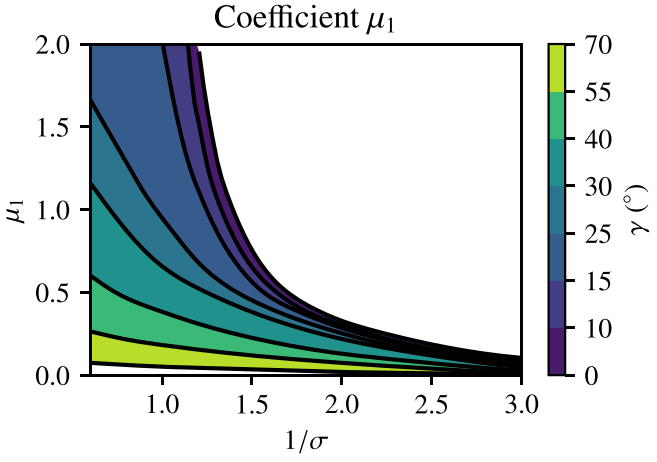

Fig. 7. Contours of interpolated Weinel relation coefficient μ_1.

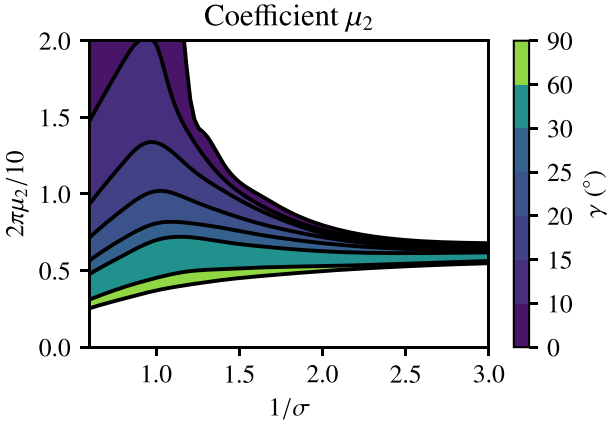

Fig. 8. Contours of interpolated Weinel relation coefficient μ_2.

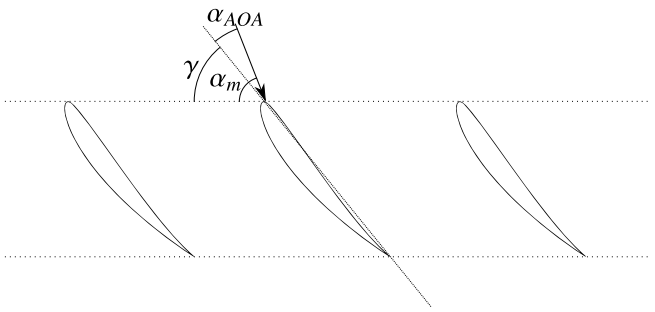

Fig. 9. Angles relations on cascades.

$$\alpha_m = \gamma_S + \alpha_{AOA,S} \tag{15}$$

$$\beta_m = \gamma_R + \alpha_{AOA,R} \tag{16}$$

To design at minimum aerodynamic loss on the cascades, this work adopts the Mataix and Alonso [24] criterion of optimal cascade operation. It consists in choosing as optimal lift coefficient of the cascade $C_{L,\text{opt}}$, the lift coefficient at maximum lift-to-drag ratio C_L/C_D of the isolated airfoil. A summary of the optimal criterion is shown in Eq. 17.

$$C_{L,\text{flw}} = C_{L,\text{geo}} = C_{L,\text{opt}} = C_{L,\text{isolated airfoil}} @ \left.\frac{C_L}{C_D}\right|_{\text{maximum}} \tag{17}$$

From Eqs. 10, 12, 14 and 15 and the optimal criterion 17, a set of equations to solve the dimensionless geometric parameters of the stator cascade can be built. The set is shown in Eq. 18, composed by 4 independent nonlinear equations and 5 unknowns (f, α_m, γ_S, $\alpha_{AOA,S}$, σ_S), a numerical function that relates any two variables can be found. The final relations to be included in the chart are shown in the set of Eqs. 19.

$$\begin{cases} \alpha_m & = \mathrm{F}_1(f) & \text{Eq.12} \\ \alpha_m & = \mathrm{F}_2(\gamma_S, \alpha_{AOA,S}) & \text{Eq.15} \\ C_{L,\text{opt},S} & = \mathrm{F}_3(\sigma_S, f) & \text{Eq.10} \\ C_{L,\text{opt},S} & = \mathrm{F}_4(\sigma_S, \gamma_S, \alpha_{AOA,S}, C_{L0,S}) & \text{Eq.14} \end{cases} \tag{18}$$

$$\begin{cases} \gamma_S(f) \\ \sigma_S(f) \\ \alpha_{AOA,S}(f) \end{cases} \tag{19}$$

Likewise, from Eqs. 11, 13, 14 and 16 and the optimal criterion 17, a set of equations to solve the dimensionless geometric parameters of the rotor cascade can be built. The set is shown in Eq. 20, composed by 4 independent nonlinear equations and 6 unknowns ($f, \psi_u, \beta_m, \gamma_R, \alpha_{AOA,R}, \sigma_R$), a numerical function that relates any three variables can be found. The final relations to be included in the chart are shown in the set of Eqs. 21.

$$\begin{cases} \beta_m & = \mathrm{G}_1(f, \psi_u) & \text{Eq.13} \\ \beta_m & = \mathrm{G}_2(\gamma_R, \alpha_{AOA,R}) & \text{Eq.16} \\ C_{L,\text{opt},R} & = \mathrm{G}_3(\sigma_R, f, \psi_u) & \text{Eq.11} \\ C_{L,\text{opt},R} & = \mathrm{G}_4(\sigma_R, \gamma_R, \alpha_{AOA,R}, C_{L0,R}) & \text{Eq.14} \end{cases} \tag{20}$$

$$\begin{cases} \gamma_R(f, \psi_u) \\ \sigma_R(f, \psi_u) \\ \alpha_{AOA,R}(f, \psi_u) \end{cases} \tag{21}$$

The chart functional signature can be expressed as shown in Eq. 22. It shows that the chart can be built from the isolated airfoil information of the stator and rotor, i.e. the lift coefficients at zero angle of attack and at optimal operation. The built chart shows variables that are function of the dimensionless factors of choice. From the chart, the dimensionless characteristics of the rotor and stator cascades can be obtained.

$$\begin{aligned} &(C_{L0,S}, C_{L,\text{op},S}, C_{L0,R}, \quad C_{L,\text{op},R}) \rightarrow \\ &\text{Chart}(f, \psi_u) \rightarrow (\sigma_S, \gamma_S, \sigma_R, \gamma_R) \end{aligned} \tag{22}$$

The algorithm to build the chart is given within the design method algorithm in the following section.

2.4. Design method algorithm

The proposed algorithm is decomposed in a five step process. Each step is detailed in the following sections.

2.4.1. Design parameters and dimensionless design space

The input parameters to the design must be selected so that they can be used to calculate the dimensionless parameters of choice (Eqs. 5 and 6 given Eq. 7).

The minimal set of parameters are the useful head H_u, the tangential speed U and the axial speed C_a. This set of parameters would need extra criteria to complete the geometrical definition of the turbine, and does not clearly translate to the practical needs on an industrial design. A more practical set of parameters are the following:

- Three operational parameters:
  - The flow rate Q.
  - The useful head H_u or mechanical power $\dot{W}$ or the total head H. These variables can be related to each other using the Eqs. 23 and 24 of the hydraulic efficiency η_h and the 3D effects efficiency η_{3D}. For small in-pipe turbines, our own experience and similar tested turbines found in the literature [11,13,28,29] shows that both efficiency values can be estimated on the range of 60–70%. Reference values are given on the design example.
  - The angular speed n.
- Two geometrical parameters that define the annular passage of the turbine:
  - The pipe size (D_p or R_p), or the hub size (D_h or R_h).
  - Given the previous one, the other element size (pipe or hub). Or a dimensionless meaningful variable like the hub-to-tip ratio T (Eq. 4) or the area factor f_A (Eq. 3).

$$\eta_h = \frac{\dot{W}}{\rho g H Q} = \frac{H_{u,3D}}{H} \tag{23}$$

$$\eta_{3D} = \frac{H_{u,3D}}{H_u} \tag{24}$$

On this work, the preferred set of design parameters are: The flow rate Q, the useful head H_u, the angular speed n, the pipe radius R_p and the area factor f_A. From now on, all the derived equations and approximations will be put as function of this set of parameters. If other set of parameters are used, the Eqs. 3, 4, 23 or 24 can be used to do the conversion between them.

Choosing the values of all five input design parameters fixes the dimensionless parameters of choice, and from that a single aerodynamically optimal design can be obtained. On this work it is proposed to soften the restriction on a maximum of two input parameters (referred as soft constraints X_1, X_2), allowing this way the selection of the final design from a set of aerodynamically optimal turbines using other criteria, like the improvement in off-design performance or cascades geometrical restrictions. The other parameters (three to four) must be fixed and are referred as hard constraints.

The selection of the parameters to be set as soft or hard constraints are case dependents. On the case where the flow conditions on the pipe and its size are known and fixed, then the flow rate Q, total head H and pipe size R_p must be set as hard constraints while the angular speed n and area factor f_A can be set as the softer ones. Another scenario that can be conceived is when designing a family of turbines over the mechanical power $\dot{W}$ or operational flow rate Q, in which case it would be needed to soften the corresponding parameter and hence hardening other parameters like the angular speed.

Given any two input design parameters chosen as soft constraints (X_1, X_2) a set of two parametric equations can be expressed as shown in Eq.

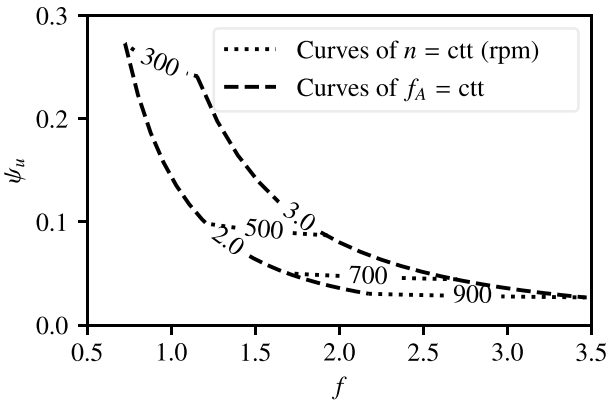

Fig. 10. Example of design space region curves using as hard constraints $Q = 30\ \mathrm{m}^3/h$, $H_u = 0.2$ m, $R_p = 0.1$ m and soft constraints $X_1 = n \in [300, 900]$rpm and $X_2 = f_A \in [2, 3]$.

25. This equations trace a region of all possible pairs (f, ψ_u) within the restrictions imposed by the hard constraints and the chosen soft constraints. The Fig. 10 shows the resulting design space contours for an example set of hard constraints (Q, H_u, R_p) and soft constraints $(X_1 = n, X_2 = f_A)$.

$$\begin{cases} f(X_1, X_2) = \dfrac{Q}{A_{\text{passage}}}\dfrac{U}{gH_u} = \dfrac{Q(n\,\pi/30)}{2\pi g H_u R_p\left(1-\sqrt{1-1/f_A}\right)} \\ \psi_u(X_1, X_2) = \dfrac{gH_u}{U^2} = \dfrac{4gH_u}{\left((n\,\pi/30)R_p\left(1+\sqrt{1-1/f_A}\right)\right)^2} \end{cases} \tag{25}$$

2.4.2. Stator and rotor airfoils characteristics

The minimal information needed from the blade cascades airfoils to be selected are the lift coefficients shown in the Weinel relation (Eq. 14). The lift coefficient at zero angle of attack C_{L0} depends on the shape of the airfoil, meanwhile the optimal lift coefficient $C_{L,\text{opt}}$ is related to the optimal operational point given by the Mataix and Alonso [24] criterion (Eq. 17). It is recommended to select the airfoils and its optimal operational point of both stator and rotor cascades independently.

On this work, based on the aerodynamic theory and the main objectives of the presented method, we suggest the following criteria when selecting the best airfoils shapes for the blade cascades:

- Highest aerodynamic performance (C_L/C_D).
- High tolerance to turbulence (little change on aerodynamic performance given high range of turbulence conditions).
- Ease of manufacturing.

Aerodynamic performance can be very sensitive to the Reynolds number (Eq. 26). Given that the actual Reynolds number depends on the mean flow speed on each cascade, it is not known a priori. The Reynolds number on the stator airfoil can be estimated approximating the mean speed to the incoming axial speed as shown in Eq. 27. For the rotor, the mean speed can be estimated assuming that angular speed dominates as shown in Eq. 28.

$$\mathrm{Re}_l = \frac{C_m l}{\nu} \tag{26}$$

$$\mathrm{Re}_{l,S} \approx \frac{C_a l}{\nu} = \frac{Q}{\pi R_p^2 f_A}\frac{l}{\nu} \tag{27}$$

$$\mathrm{Re}_{l,R} \approx \frac{\omega R_m l}{\nu} = \frac{n\left(\pi/30\right)R_p\left(1+\sqrt{1-1/f_A}\right)}{2}\frac{l}{\nu} \tag{28}$$

Given that the Reynolds number depends on the chord length l, a structural criterion must be chosen for the blades. On this work, the criterion is based on the selection of the aspect ratio as shown in Eq. 29. Also its important to take in account the blade construction distortion when selecting the aspect ratio. Form a detailed geometric analysis the distortion (Eq. 30) can be deduced. Both equations can be combined to obtain the minimal aspect ration (Eq. 31).

$$\mathrm{ar} = \frac{R_p - R_h}{l} \Rightarrow l = R_p\frac{1-\sqrt{1-1/f_A}}{\mathrm{ar}} \tag{29}$$

$$\epsilon = \left.\frac{l_{\text{cyl proj}} - l_{\text{flat proj}}}{l_{\text{cyl proj}}}\right|_{\gamma=0} \simeq \frac{1}{24}\left(\frac{1}{\mathrm{R_m}}\right)^2 \tag{30}$$

$$\mathrm{ar}_{\min} = \frac{1-\sqrt{1-1/f_A}}{1+\sqrt{1-1/f_A}}\frac{1}{\sqrt{6\epsilon}} \tag{31}$$

Given the imposed criteria for the bi-dimensional cascade theory of $f_A \geqslant 2$, and a maximum distortion of $\epsilon = 2\%$, the minimum aspect ratio becomes 0.5.

Aerodynamic performance can be sensitive to turbulence levels of the mean flow. On that case, an estimation of the turbulence intensity on the turbine passage must be calculated. To get an order of magnitude, it can be approximated to the arithmetic mean turbulence on the pipe upstream [30] (Eq. 32).

$$I_p = 0.277\ \mathrm{Re}_p^{-0.1} \tag{32}$$

If the involved variables on the estimation of the Reynolds numbers are part of the soft constraints, no single value can be calculated. On this case the mean Reynolds number on the design space is chosen to be taken as reference.

Given the reference Reynolds number, a parametric study of the performance curves of the considered set of airfoils shapes can be made. From that study, the lift coefficient at zero angle of attack C_{L0} and the optimal lift coefficient $C_{L,\text{opt}}$ for the stator and rotor can be obtained.

2.4.3. Dimensionless design chart algorithm

To build the chart, the steps bellow must be followed:

1. The airfoils for the stator and rotor must be previously selected. The lift coefficients at zero angle of attack $C_{L0,S,R}$ can be obtained from them.
2. Following the criterion in Eq. 17, the optimal lift coefficients $C_{L,\text{opt},S,R}$ can be obtained.
3. The equations on the set 20 can be numerically solved to obtain the interpolating functions on set 21. The obtained functions being dependent on two variables can be plotted as contour surfaces. The flow-to-head factor f is chosen to be placed on the horizontal axis. The angle of attack function $\alpha_{AOA,R}$ is chosen to be represented as a color filled contour, while the other variables to be represented as contour lines.
4. The equations on the set 18 can be numerically solved to obtain the interpolating functions on set 19. Given that the functions depends on the flow-to-head variable, they are chosen to be represented as nonlinear horizontal axis parallel to it. A very compact chart is obtained. This concludes the building of the chart.

An example chart is shown in Fig. 11. It clearly shows the contours for the solved equations in set 21 and the mapped nonlinear horizontal axis for the solved equations in set 19.

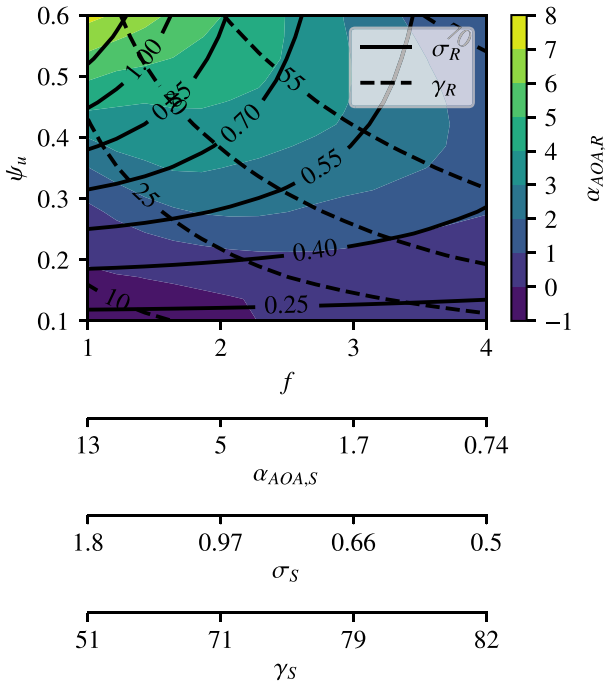

Fig. 11. Example of a dimensionless design chart using $C_{L0,S} = 1, C_{L,\text{opt},S} = 1$, $C_{L0,R} = 1, C_{L,\text{opt},R} = 1$.

2.4.4. Selection of the turbine on the dimensionless design chart

From the previously built dimensionless design chart, and from the design space curves (Eqs. 25) a combined chart can be made (ex. combining Figs. 10 and 11). A full chart is built and shown in the design example section.

To select the final design from the design space, the following recommendations are given:

- To pick the design that reduce the angle of attack on both stator and rotor cascade, improving the off-design characteristics (specially for very fast turbines).
- To have a solidity $\sigma > 0.25$, limiting this way the minimum number of blades. This bound the maximum aerodynamic load on the individual blades and hence improves the aerodynamic performance. A more strict criterion could be imposed.
- As reference, it can be chosen to meet the usual criterion of specific speed on propeller turbines [21], i.e. $\Omega_s \in \{2,3\}$. The specific speed contours can be plotted using Eq. 33.

$$\Omega_s\left(X_1, X_2\right) = \frac{(n\,\pi/30)Q^{1/2}}{(gH_u(\eta_h/\eta_{3D}))^{3/4}} \tag{33}$$

Given all the restrictions and criteria, six parameters can be recovered from the chart: the stagger angle γ and solidity σ for both rotor and stator cascades and the two soft constraints X_1 and X_2.

2.4.5. Calculation of the turbine geometry

Given the selected turbine, the final dimensions of the cascades and the turbine passage can be calculated. If a meaningful dimensionless parameter was selected as geometric parameter of the passage, the corresponding hub or pipe size can be calculated using Eqs. 3 or 4. To calculate the chord length and number of blades of the cascades, the following criteria are imposed:

- The number of stator and rotor blades to be co-prime, assuring the least stator-rotor wake shadowing.
- Approximately meet the aspect ratio criterion given on the airfoil selection study, favoring values greater than the imposed aspect ratio.

To meet these criteria, a discrete brute force search algorithm is proposed. Other algorithms could be implemented as long as the mentioned imposed criteria could be met. The algorithm is detailed bellow:

1. Estimate the number of blades using Eq. 34 (derived from Eqs. 1 and 29).
2. Verify that the blade numbers are co-prime using the great common divisor condition (Eq. 35).
3. If they are not co-prime, increment or decrement the number of blades of one of the cascades and return to step 2).
4. Calculate the chord length using Eq. 36.
5. Calculate the aspect ratio criterion given in Eq. 37
6. If the aspect ratio criterion is not met, increment or decrement the number of blades of one of the cascades and return to step 2).
7. The algorithm finish when all conditions are met. It can be run until the aspect ratio is as close as possible to the one used in the airfoil selection study.

$$Z_{S,R} = \left\lceil \pi\sigma_{S,R}\left(\frac{1+\sqrt{1-1/f_A}}{1-\sqrt{1-1/f_A}}\right)\text{ar}\big|_{\text{airfoiln study criterion}} \right\rceil \tag{34}$$

$$\gcd(Z_S, Z_R) = 1 \tag{35}$$

$$l_{S,R} = \pi\sigma_{S,R}\frac{R_p\left(1+\sqrt{1-1/f_A}\right)}{Z_{S,R}} \tag{36}$$

$$\text{ar}_{S,R} = R_p\frac{1-\sqrt{1-1/f_A}}{l_{S,R}} \gtrapprox \text{ar}\big|_{\text{airfoil study criterion}} \tag{37}$$

To complete the geometric definition of the turbine, the proportions of the bulb and the distance between the cascades must be defined. On the design example reference proportions are given.

Additionally, the rotor tip gap must be defined. As reference, Dixon [21] affirms that for each 1% of clearance gap to blade height, about 2 to 3% of efficiency is lost.

To this point, the complete definition of the turbine has been obtained.

3. Design example

To better compare the characteristics of the turbines designed with the presented method, a design example is made on similar conditions as the 5BTP pico propeller turbine [11].

3.1. Design constraints

The design constraints are shown on Table 1. They have been chosen around the best efficiency point of the reference turbine. To allow a direct comparison between designs, the size and conditions on the pipe have been set as hard constraints, hence the angular speed and the area

Table 1
Input parameters for the design example.

		Values
Operational parameters	Q (m^3/h)	16
	H ($m.w.c$)	0.34
	n (rpm)	[500,1500]
Geometrical parameters	R_p (m)	0.0425
	f_A	[2,3]

factor have been chosen as the soft constraints.

The useful head can be calculated using Eqs. 23 and 24 estimating the efficiencies to $\eta_h \approx 70\%$ and $\eta_{3D} \approx 65\%$, obtaining $H_u \approx 0.37$m.w.c.

3.2. Stator and rotor selection study

To select the airfoils, the following criteria were applied:

- Arc of circle shape for ease of manufacturing.
- Aspect ratio (Eq. 29) ar ≈ 0.6 to assure structural robustness.
- Blade thickness thk$\geqslant$1mm to impose a secondary structural criterion for the specific family of airfoils to be studied.
- Airfoil camber that maximize C_L/C_D over an large range of angles of attack.

To select the optimal airfoils relative camber h/l and the optimal lift coefficient $C_{L,\text{opt}}$ a parametric study using XFOIL [31] was made. To be able to study the airfoils, the relative thickness, the Reynolds number at mean radius and the turbulent transition criteria must be estimated:

- To estimate both relative thickness and Reynolds numbers, the chord length design space was calculated using Eq. 29 given the aspect ratio criterion. The chord length space obtained was $l \in [13, 21]$mm.
- The minimum relative thickness that meets the criterion given the chord length design space was calculated, obtaining thk$/l = 0.08$.
- Reynolds number can be calculated from the approximations shown on Eqs. 27 and 28. The reference Reynolds numbers obtained from the design space where: $\text{Re}_S = 3.5e4$ and $\text{Re}_R = 7.6e4$.
- The turbulence intensity was estimated using Eq. 32, obtaining $I_p = 9.1\%$. The obtained value is very high, indicating that bypass turbulence mechanism dominates the laminar-turbulent transition. On this situation, XFOIL recommends to manually set the relative chord distance xtr$/l$ where the transition occurs. Given the values of Reynolds numbers and turbulence intensity involved, the mean turbulence transition point was set to xtr$/l = 0.1$ [32].

On Fig. 12 and 13 the stator and rotor XFOIL parametric studies with the selected optimal relative camber and lift coefficient are shown. Two plots per cascade are shown. The one on the right shows a contour plot

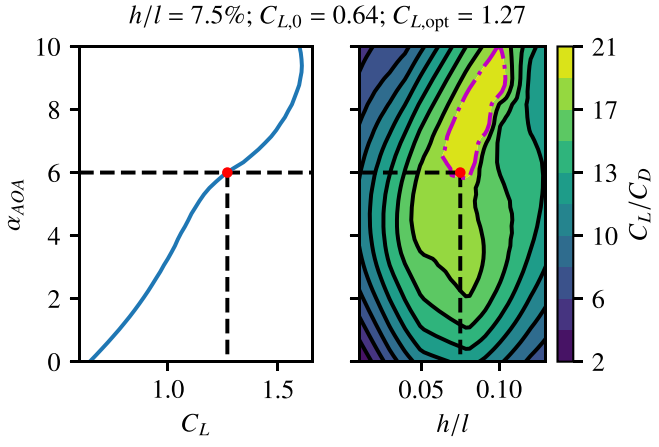

Fig. 12. Stator airfoil selection plot. At the right, the contours of aerodynamic performance as function of the angle of attack and the relative camber. At the left, the angle of attack vs lift coefficient for the selected airfoil.

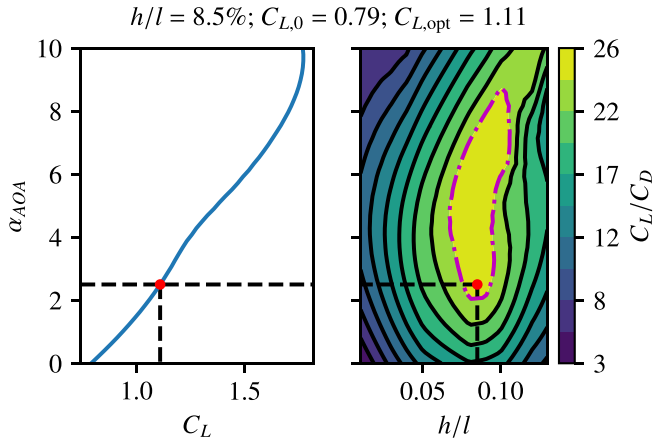

Fig. 13. Rotor airfoil selection plot. At the right, the contours of aerodynamic performance as function of the angle of attack and the relative camber. At the left, the angle of attack vs lift coefficient for the selected airfoil.

Table 2
Selected airfoils and its optimal lift coefficient for the stator and rotor cascades.

	h/l (%)	C_{L0}	$C_{L,\text{opt}}$
Stator airfoil	7.5	0.64	1.27
Rotor airfoil	8.5	0.79	1.11

with the level curves of aerodynamic performance C_L/C_D as function of the relative camber h/l and angle of attack α_{AOA}. The contour line with maximum value indicate the region where the airfoils have 90% or more performance. A dot shows the selected airfoil relative camber and the chosen optimal angle of attack. The plot on the left shows the curve of angles of attacks vs lift coefficient at the selected relative camber. The point of selected optimal lift coefficient is shown. The angle of attack vertical axis is shared by both plots.

An extra criteria is added to select of the optimal lift coefficient: To be on the plateau of 90% of C_L/C_d at reduced angle of attack, assuring a maximum span of performance on higher angles of attacks. This criterion is added to assure better performance when the turbine gets heavily loaded.

The selected airfoils and optimal lift coefficients are shown in Table 2. A dimensionless design chart can be build from the obtained lift coefficients.

3.3. Turbine selection

Additionally to the dimensionless design chart, the design space of all possible turbines given the constraints must be plotted on it. From the combined chart, a turbine can be selected given the criteria explained in previous sections. The selected soft constraints are substituted on Eqs. 25 ($X_1 = n$, $X_2 = f_A$). The specific speed Ω_s is also added on the design space region.

On Fig. 14 the dimensionless design chart with the parametric design space is shown. On the chart the selected design is marked with a dot, and cascade dimensionless parameters are showed in the title. A design is selected so it meets all the constraints. The design that fulfilled all restrictions and criteria is summarized on the Table 3.

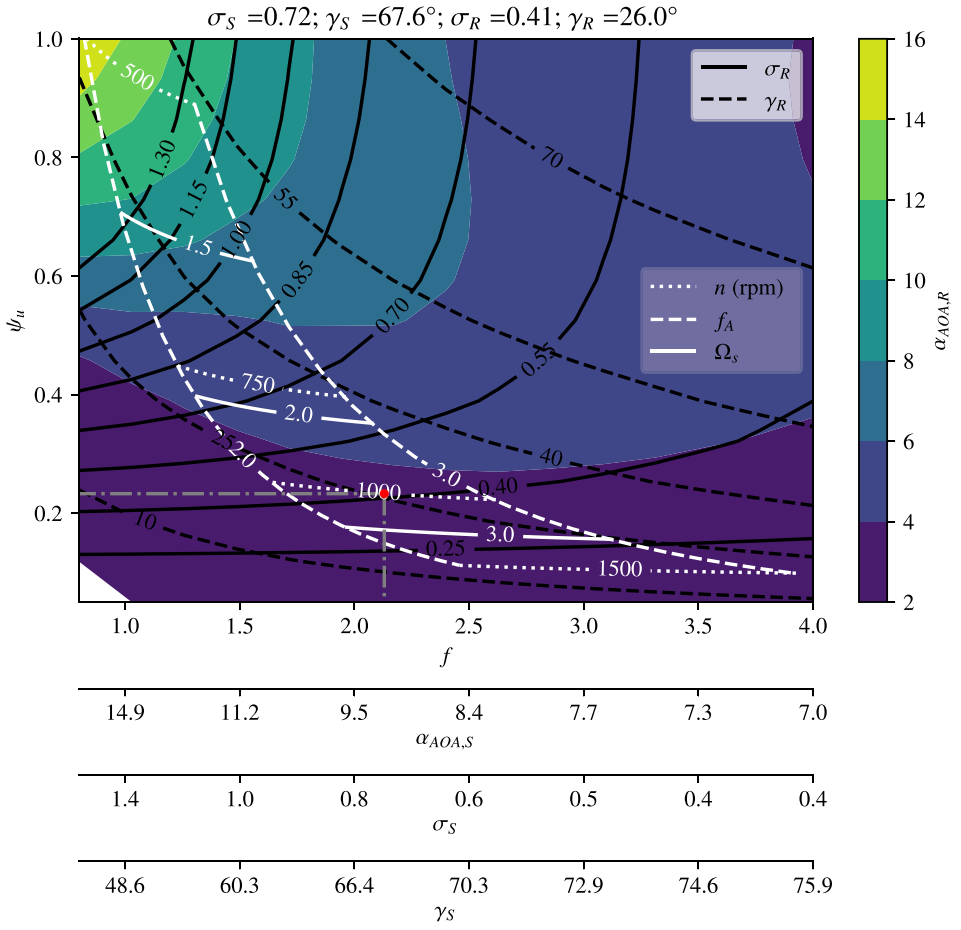

Fig. 14. Dimensionless design chart with design space surface showing the selected turbine.

Table 3
Summary of the selected design.

		Values
Stator dimensionless cascade and airfoil	σ	0.72
	γ (°)	67.6
	thk/l (%)	8.0
	h/l (%)	7.5
Rotor dimensionless cascade and airfoil	σ	0.41
	γ (°)	26.0
	thk/l (%)	8.0
	h/l (%)	8.5
Selected soft constriants	n (rpm)	1000
	f_A	2.5
Dimensionless point	f	2.1
	ψ_u	0.23
	Ω_s	2.5

3.4. Turbine geometry

To completely obtain the geometric dimensions of the turbine, the turbine passage, chord lengths, number of blades and bulb shape must be calculated. The passage size can be obtained from the pipe radius R_p and area factor f_A, so the hub radius R_h can be calculated (Eq. 3). The obtained hub radius was: $R_h = 0.0329$m.

The chord length l and the number of blades Z was calculated according to the criteria exposed on the sections before, given the structural criteria of having an aspect ratio greater but approximately equal to 0.6. The corresponding calculations resulted in the values summarized in Table 4.

To obtain the bulb proportions proposed for this example, a simple computational fluid dynamics study not shown here was made. The obtained proportions that minimized the energy losses are shown on Fig. 15. The upstream and downstream perturbation caused by the cascades it is assumed to be negligible after a chord length distance up and downstream from the edges of the profiles [21]. This criterion is used to choose the axial width of the cascades.

The rotor tip gap to blade height was chosen to be 5%. The reason behind this choice is to loosen the tolerances as much as possible to ease manufacturing.

Table 4
Calculated blade row characteristics for the stator and rotor.

	Z	l (m)	ar_{final}
Stator row	11	0.0155	0.62
Rotor row	7	0.0139	0.69

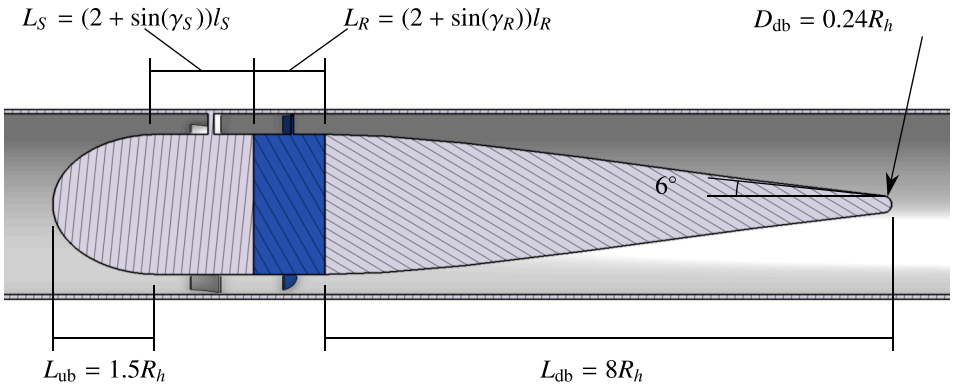

Fig. 15. Bulb proportions for the design example.

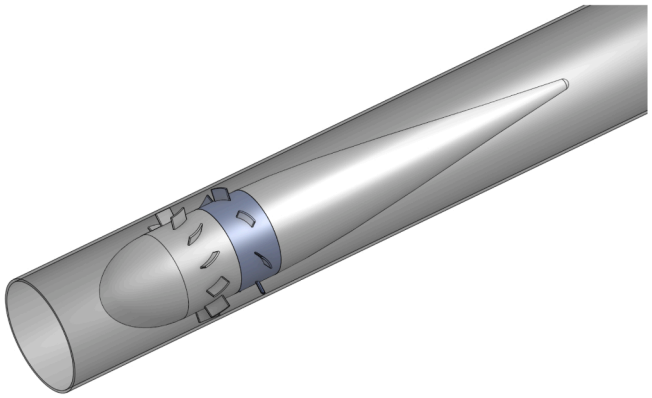

Fig. 16. Geometry of the designed turbine.

The complete solid geometry of the designed turbine to be simulated is shown in Fig. 16.

The summary of the designed turbine is shown in Table 5. Additionally to all previously calculated dimensionless and geometric parameters, the maximum constructive distortion of the blade is shown (Eq. 30).

4. Numerical analysis

To show the behavior of the designed turbine, simulations are carried over and the resulting efficiency curve is compared to the reference turbine (5BTP). A validation of the mesh and numerical settings is performed to ensure the quality of the results.

The mesh other than the blade rows volumes have been obtained with the open source software Salome platform v9. For the blades rows high quality meshes were obtained with Ansys® TurboGrid v17. All simulations have been obtained using the open source library OpenFOAM v8.

4.1. Numerical validation

For the numerical validation it was used as reference the turbine described by Shigemitsu et al. [29] [28]. On this reference case, a pico-hydraulic counter rotating turbine is simulated and experimentally tested. On this work, a parametric mesh study is developed to choose the best meshing characteristics to use on the design example simulations. A comparison with the experimental results of the reference validation case is also performed.

The computational domain is shown in Fig. 17. It can be noticed that the fluid volumes of the domain are separated in five regions: inlet and outlet regions, front and rear rotor blade rows regions and spoke region.

Table 5
Summary of designed turbine.

		Values
Chosen dimensionless point	f	2.1
	ψ_u	0.23
	Ω_s	2.5
Design parameters	$Q\ (m^3/h)$	16
	$H_u\ (m.w.c)$	0.37
	n (rpm)	1000
	$R_p\ (mm)$	42.5
	f_A	2.5
Stator airfoil and cascade characteristics	thk/l (%)	8.0
	h/l (%)	7.5
	σ	0.72
	γ (°)	67.6
	$l\ (mm)$	15.5
	Z	11
	ϵ (%)	0.7
Rotor airfoil and cascade characteristics	thk/l (%)	8.0
	h/l (%)	8.5
	σ	0.41
	γ (°)	26.0
	$l\ (mm)$	13.9
	Z	7
	ϵ (%)	0.6
Geometric dimensions	$R_h\ (mm)$	32.9
	L_{ub} (mm)	49.4
	L_S (mm)	45.3
	L_R (mm)	33.9
	L_{db} (mm)	263.2
	D_{db} (mm)	7.9
	gap (mm)	0.5

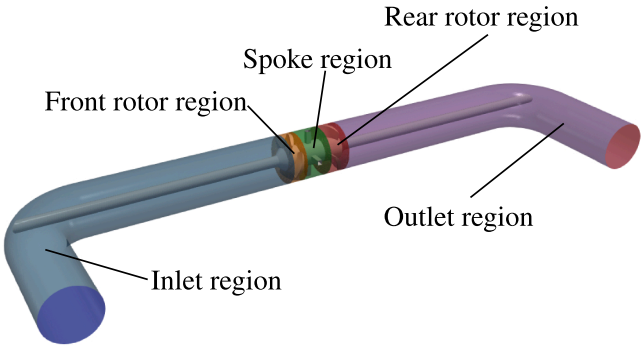

Fig. 17. Computational domain of the validation case.

Table 6
Parameters of mesh study for the blade row regions.

Mesh	y^+	Global size factor		Cell count
		Front rotor	Rear rotor	
coarse	1.4	0.65	0.638	7 170 948
medium	1.00	1.06	0.985	20 112 092
fine	0.71	1.71	1.500	56 110 066

Table 7
Parameters of mesh study for the inlet, outlet and spoke regions.

Mesh	y^+	Max elem. size factor			Cell count
		Inlet	Outlet	Spoke	
coarse	60	1.46	1.46	1.39	3 032 311
medium	42.9	2.00	1.69	1.06	8 431 187
fine	30.6	1.41	1.48	1.34	23 116 691

Table 8
Total number of elements.

Mesh	Cell count
coarse	10 203 259
medium	28 543 279
fine	79 226 757

The blade row regions where meshed with Ansys® TurboGrid with hexahedral multi-block mesh strategy, while the other regions where meshed with open source Salome platform with tetrahedral unstructured mesh strategy.

Three meshes where made to estimate the discretization uncertainty using the Roache's grid convergence index (GCI) [33,34]. The effective ratio r (Eq. 38) for each region was enforced to be 1.4. Additionally, for the inlet, outlet and spoke interfaces to the blade row regions, the element size was forced to be equal to the mean bulk flow element size on the rotor flow region side. A summary of the parameters and the resulting meshes is presented in Tables 6 and 7. The y^+ parameter was used as reference and varied proportional to the effective ratio r, while the size factors were adjusted to obtain the desired mesh sizes. A summary of the total number of elements for each mesh is shown in the Table 8. On Fig. 18 the medium mesh is shown, detailing the characteristics of the generated mesh.

$$r = \left(\frac{N_{\text{fine}}}{N_{\text{medium}}}\right)^{\frac{1}{3}} = \left(\frac{N_{\text{medium}}}{N_{\text{coarse}}}\right)^{\frac{1}{3}} \tag{38}$$

The simulations were developed for the design flow rate Q_d of the validation case. Numerical settings that have been proved to accurately predict hydraulic turbomachinery behavior where used [13,35]. Steady state simulations were carried out with `simpleFoam` application from the OpenFOAM library. Rotating regions where modeled with the multi reference frame (MRF) approach. All interfaces where non-conformal and coupled with `cyclicAMI` boundary condition (BC). For the inlet BC fixed uniform velocity was set, while for the outlet BC fixed uniform pressure. Turbulence model was set to the omega SST. Wall functions where used on inlet, outlet and spoke regions, while a near wall low-Reynolds modeling was used for the blade row regions. The discretization schemes where set second order for the velocity field and first order for the viscosity. The convergence criteria was the stabilization of pressure head (difference between inlet and outlet pressure) and the mechanical power delivered by the blade rows for at least 1000 iterations.

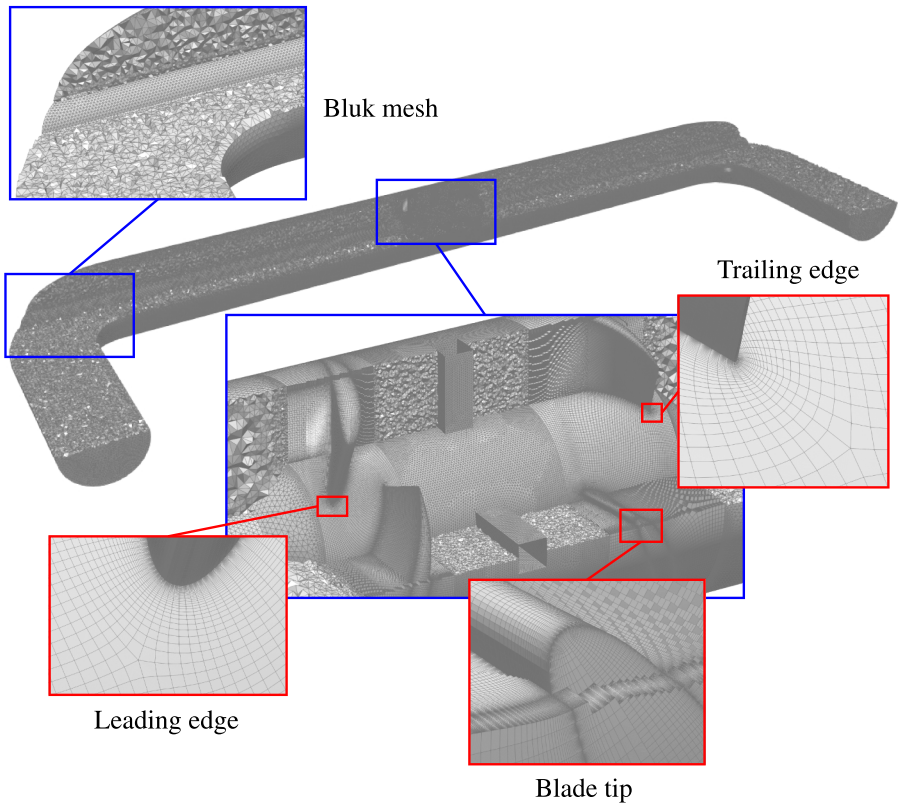

Fig. 18. Details of the medium mesh.

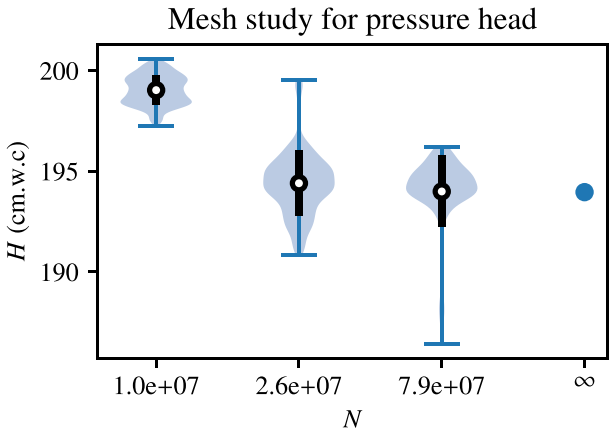

Fig. 19. Pressure head for different mesh sizes showing violin plot of value oscillations over 1500 iterations. The standard deviation error bars are indicated with a thick line around the mean values. The asymptotic value of Richardson extrapolation is shown.

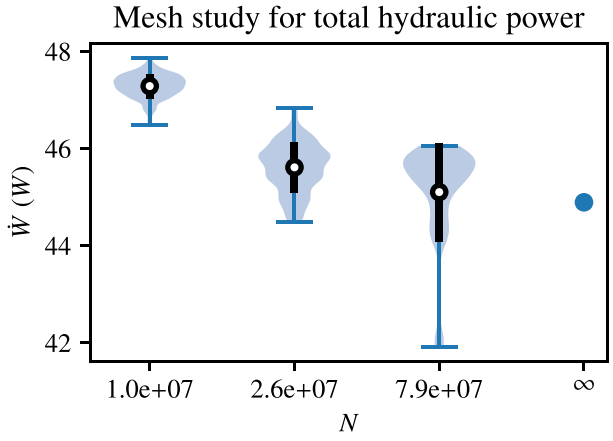

Fig. 20. Total mechanical power for different mesh sizes showing violin plot of value oscillations over 1500 iterations. The standard deviation error bars are indicated with a thick line around the mean values. The asymptotic value of Richardson extrapolation is shown.

On Figs. 19 and 20, the results of the simulations for the pressure head H and the mechanical power $\dot{W}$ are shown. Convergence oscillations and Richardson extrapolations were represented on them. The CGI for the coarse and medium size meshes are shown in the Table 9. The discretization uncertainty on the medium size mesh is considered reasonably small and its related parameters are chosen to be used as reference for further simulations. The uncertainty on the pressure head H and mechanical power $\dot{W}$ can be propagated to the hydraulic efficiency η_h, finding an uncertainty of $\approx 1\%$.

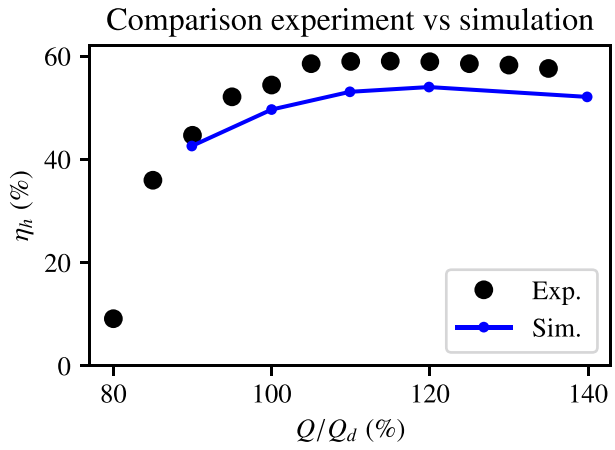

Fig. 21. Comparison between the experimental results of the reference case and the simulations with the medium size mesh.

Given the chosen mesh and numerical setup, simulations were carried over to reproduce the hydraulic efficiency curve. The Fig. 21 shows the numerical results superimposed with the experimental results of the validation case. It can be noticed that the simulations reproduce the curve behavior, and underestimated the total value with less than 10% error. The differences on maximum efficiency can be due to small deviations between the manufactured turbine and the information given for its geometric reconstruction.

4.2. Design example numerical simulation

The simulations were carried over the domain shown in Fig. 22. It is divided in four regions: inlet, outlet, stator and rotor blade rows. The inlet is set $2D_p$ upstream the stator cascade, and the outlet $8D_p$ downstream the rotor cascade. Given that the downstream supports where not part of the design study, they are not included on the simulations.

The mesh characteristics follows the medium mesh of the validation case. A summary is shown in Table 10.

Steady state simulations with MRF approach (rotor region) where carried over with the same settings as the validation case. Exceptions to this rule were the inlet and outlet boundary conditions. Given the short

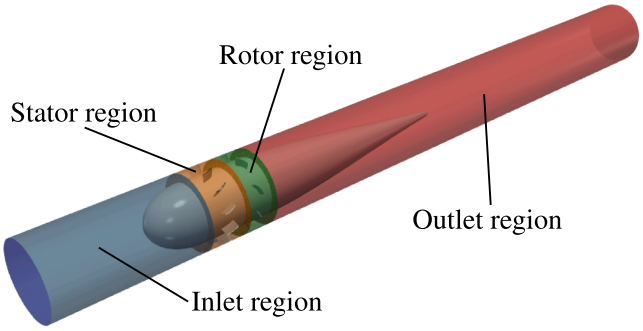

Fig. 22. Computational domain of the designed turbine.

Table 9
Grid convergence index results for the mesh study.

variables	coarse	medium	fine	asymptotic value	GCI_{medium} (%)	GCI_{coarse} (%)
H $(cm.w.c)$	199.0	194.4	194.0	193.96	0.3	3.2
$\dot{W}$ (W)	47.3	45.6	45.1	44.89	1.9	6.6

Table 10
Mesh characteristics for the design example simulations.

	Values
Blade Rows	
y^+	1
Global size factors	1
Cell count	4 796 414
Inlet/Outlet	
y^+	42.9
Max. elem. size factor	1.58
Cell count	11 883 395
Total cell count	16 679 809

distance on the inlet, a developed flow power law velocity profile was imposed. For the outlet, the mean pressure was fixed, allowing the development of a radial pressure gradient given the expected swirling velocity field.

4.3. Results and discussion

From the simulations the minimum information to reconstruct the complete behavior of the turbine was recovered and represented, i.e. the hydraulic efficiency η_h and the pressure head H. The results where compared with the 5BTP reference turbine working at 1000rpm. This speed was chosen because it spans the widest flow rate range and matches the machine Reynolds number of the design (Eq. 39).

$$\mathrm{Re}_{\mathrm{machine}} = \frac{\omega D_p^2}{\nu} \tag{39}$$

The comparison is shown in the Fig. 23. The maximum efficiency found was 65%, which is on the expected range for this kind of turbines. The design point is correctly predicted, given the optimal aerodynamic criteria shown in Figs. 13 and 12, being the design efficiency set at the beginning of the 90% performance plateau. The obtained efficiency at the design point was $\eta_h = 61\%$, which is lower than the assumed for the design inputs; in consequence a higher pressure head is obtained ($H = 42$cm.w.c). The efficiency curves shows that the designed turbine have similar efficiency curve behavior on the max efficiency plateau, but it quickly loses performance for higher flow rates. It is important to notice that it has a gentler pressure head curve, which meas that it tends to block less the pipe for a wider range of operation.

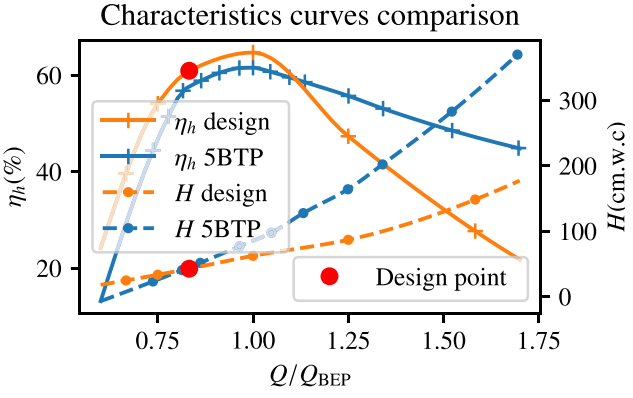

Fig. 23. Characteristics curves comparison. Design BEP flow rate 19.2 m^3/h. 5BTP@1000 rpm BEP flow rate 23.5 m^3/h.

5. Conclusion and recommendations

The design method was explained and applied to a design example case. The produced dimensionless design chart is shown to be compact, and allows the fast design of families of tailored pico-hydraulic turbines as long as the airfoil shapes remains unchanged. The blade simplicity embedded on the design hypothesis allows a reduction in manufacturing complexity and the use of the advanced bi-dimensional cascade theory for the constructions of the chart allows to obtain an optimal design despite such simple blades. The obtained turbines are simple, self contained, tubular and torpedo-shaped, ideal to be simply plugged in pipe networks sections where needed.

From the parametric study of the mesh uncertainty: a $y+ = 1$ and a global size factor of 1 on Ansys TurboGrid® for the meshing of the blade rows as well as a $y^+ = 42.5$ and maximum element factor of 1.58 for the meshing of the rest of the domain using Salome platform, is shown to produce maximum mesh uncertainty of about one point of the hydraulic efficiency.

From the simulation results, a maximum hydraulic efficiency of $\approx$ 65% shows that the designed turbines are on the expected efficiency ranges. The off-design curves shows that for very high flow rates the efficiency drops faster than other designs, but the plateau of efficiency is about the same size as the compared design.

The recommendations on further improvements include:

- A complete study on the aspect ratio and rotor blade tips effects.
- A study on the downstream bulb supports, and design recommendations.
- A more complete modeling of the isolated to cascade correlation, including low Reynolds number effects and cascade drag coefficient.
- A detailed study to improve accuracy of the estimation of the values of the hydraulic efficiency and 3D effects efficiency used as inputs for the method.

A more advanced design method that would include the strict imposition of the radial equilibrium hypothesis is expected to show better performances, but it would requiere the twisting of the blades, and hence rise the complexity of the manufacturing.

Data availability

Adhering to FAIR guidelines promoted by the European commission [36], the code for the method's algorithm, the generated meshes, simulation settings and numerical results have been made available on open-access repositories [37–39].

CRediT authorship contribution statement

Abraham Vivas: Conceptualization, Methodology, Software, Validation, Formal analysis, Investigation, Data curation, Writing – original draft, Visualization. **A. Viedma:** Conceptualization, Formal analysis, Writing – review & editing, Supervision, Funding acquisition. **A.S. Kaiser:** Conceptualization, Validation, Resources, Project administration, Funding acquisition.

Declaration of Competing Interest

The authors declare that they have no known competing financial interests or personal relationships that could have appeared to influence the work reported in this paper.

Acknowledgments

This work have been supported by Fundación Séneca (Murcia, Spain) [Grant No. 20352/FPI/17].

Appendix A. Flow lift coefficients

The Kutta-Joukowsky theorem applied to a blade cascade can be deduced from energy and momentum balances as shown in [21,24,40]. The resulting expression (Eq. A.1) relates the total force F_L (lift force) to the mean speed C_m and other parameters. The mean speed is defined as in Eq. A.2.

$$F_L = \rho \Gamma C_m = \rho t \Delta C_\theta C_m \tag{A.1}$$

$$\overrightarrow{C}_m = \frac{\overrightarrow{C}_1 + \overrightarrow{C}_2}{2} \tag{A.2}$$

On blade cascades, analogous to an isolated airfoil, the lift coefficient is defined as shown in Eq. A.3. The flow lift coefficient of the cascade (Eq. A.4) can be obtained by the nondimensionalization of Eq. A.1 with the definition in Eq. A.3.

$$C_L = \frac{F_L}{\frac{1}{2}\rho C_m^2 l} \tag{A.3}$$

$$C_{L,\mathrm{flw}} = 2\left(\frac{t}{l}\right)\left(\frac{\Delta C_\theta}{C_m}\right) = 2\frac{\Delta C_\theta}{\sigma C_m} \tag{A.4}$$

The cascade configuration used in the design method (stator-rotor), and velocity triangles are shown in Fig. A.24. The stage hypothesis of axial inlet and outlet velocity is shown. Velocity triangles can be made dimensionless dividing their magnitudes by the tangential speed U. Additionally, the change in the tangential component of absolute velocity in the stator ΔC_θ and relative velocity in the rotor ΔW_θ are the same and can be related to the useful head factor ψ_u as shown in Eq. A.5. Likewise, the flow factor ϕ can be related to the axial speed C_a as shown in Eq. A.6.

$$\frac{\tau_u \omega}{\dot{m}} = U \Delta W_\theta = g H_u \Rightarrow \frac{g H_u}{U^2} = \frac{\Delta W_\theta}{U} = \frac{\Delta C_\theta}{U} = \psi_u \tag{A.5}$$

$$\frac{C_a}{U} = \phi \tag{A.6}$$

To summarize the velocity triangles, a trapezoidal-like scheme with the dimensionless velocity triangles can be build as shown in Fig. A.25. It allows to concisely visualize the constraints and relations between the most relevant dimensionless variables.

From Fig. A.25, absolute and relative dimensionless mean speeds ($C_m/U, W_m/U$) can be related to the useful head and flow factor as shown in Eqs. A.7 and A.8 respectively. Combining this equations with Eqs. A.5 and A.4, the flow lift coefficients for the stator and rotor cascades can be related to the dimensionless useful head and flow factors. To simplify further the stator flow lift coefficient, a novel flow-to-head factor is defined as shown in Eq. A.9. The final expression for both flow lift coefficients (stator and rotor) are shown in Eqs. A.10 and A.11.

$$\frac{C_m}{U} = \sqrt{\phi^2 + \frac{\psi_u^2}{4}} \tag{A.7}$$

$$\frac{W_m}{U} = \sqrt{\phi^2 + \left(1 - \frac{\psi_u}{2}\right)^2} \tag{A.8}$$

$$f = \frac{\phi}{\psi_u} \tag{A.9}$$

$$C_{L,\mathrm{flw},S} = \frac{2}{\sigma_S}\left(\frac{1}{\sqrt{f^2 + \frac{1}{4}}}\right) \tag{A.10}$$

$$C_{L,\mathrm{flw},R} = \frac{2}{\sigma_R}\left(\frac{1}{\sqrt{f^2 + \left(\frac{1}{\psi_u} - \frac{1}{2}\right)^2}}\right) \tag{A.11}$$

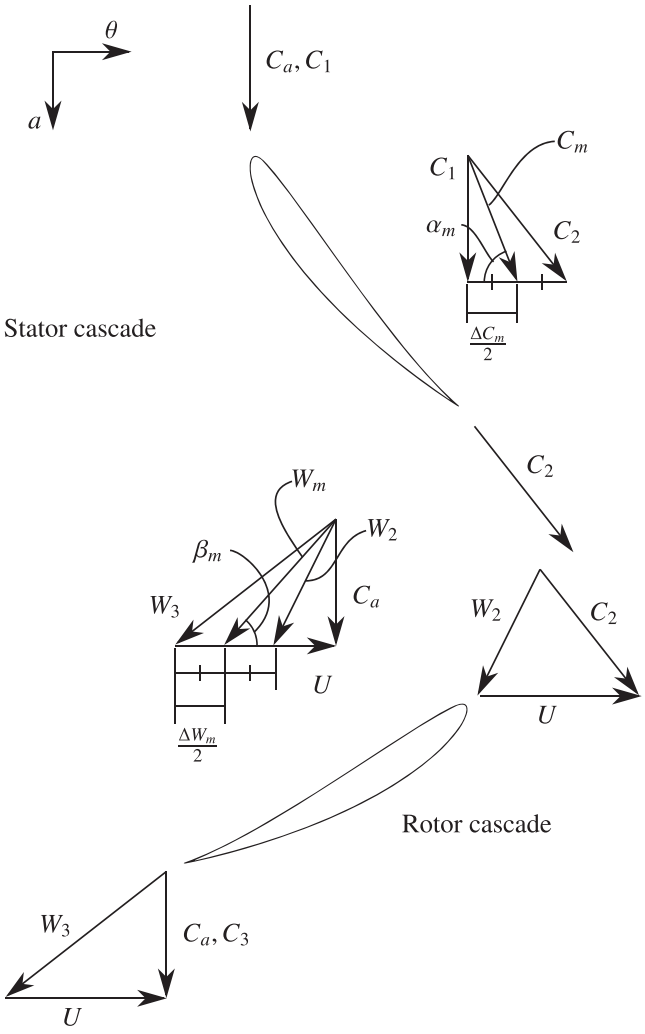

Fig. A.24. Stage configuration with velocity triangles.

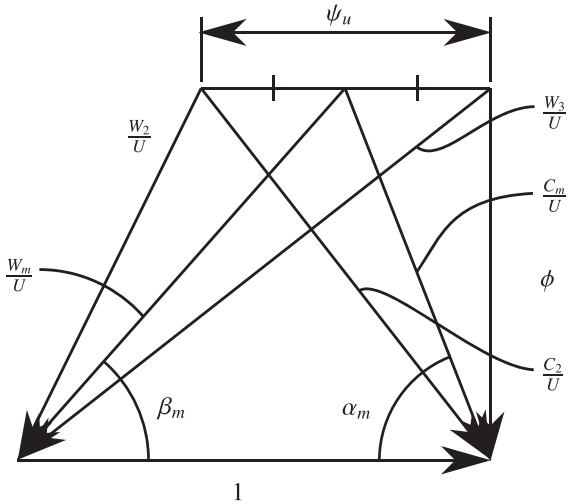

Fig. A.25. Nondimensional stage velocity triangles.

References

[1] Paish O. Small hydro power: technology and current status. Renew Sustain Energy Rev 2002;6:537–56. https://doi.org/10.1016/s1364-0321(02)00006-0.

[2] Liu X, Luo Y, Karney BW, Wang W. A selected literature review of efficiency improvements in hydraulic turbines. Renew Sustain Energy Rev 2015;51:18–28. https://doi.org/10.1016/j.rser.2015.06.023.

[3] Lahimer A, Alghoul M, Sopian K, Amin N, Asim N, Fadhel M. Research and development aspects of pico-hydro power. Renew Sustain Energy Rev 2012;16:5861–78. https://doi.org/10.1016/j.rser.2012.05.001.

[4] McNabola A, Coughlan P, Corcoran L, Power C, Prysor Williams A, Harris I, Gallagher J, Styles D. Energy recovery in the water industry using micro-hydropower: an opportunity to improve sustainability. Water Policy 2013;16:168–83. https://doi.org/10.2166/wp.2013.164.

[5] Vilanova MRN, Balestieri JAP. Hydropower recovery in water supply systems: Models and case study. Energy Convers Manage 2014;84:414–26. https://doi.org/10.1016/j.enconman.2014.04.057.

[6] Zhou D, Deng ZD. Ultra-low-head hydroelectric technology: a review. Renew Sustain Energy Rev 2017;78:23–30. https://doi.org/10.1016/j.rser.2017.04.086.

[7] Bozorgi A, Javidpour E, Riasi A, Nourbakhsh A. Numerical and experimental study of using axial pump as turbine in pico hydropower plants. Renew Energy 2013;53:258–64. https://doi.org/10.1016/j.renene.2012.11.016.

[8] Novara D, McNabola A. A model for the extrapolation of the characteristic curves of pumps as turbines from a datum best efficiency point. Energy Convers Manage 2018;174:1–7. https://doi.org/10.1016/j.enconman.2018.07.091.

[9] Delgado J, Andolfatto L, Covas D, Avellan F. Hill chart modelling using the hermite polynomial chaos expansion for the performance prediction of pumps running as turbines. Energy Convers Manage 2019;187:578–92. https://doi.org/10.1016/j.enconman.2019.02.051.

[10] Ramos HM, Simão M, Borga A. Experiments and cfd analyses for a new reaction microhydro propeller with five blades. J Energy Eng 2013;139:109–17. https://doi.org/10.1061/(asce)ey.1943-7897.0000096.

[11] Samora I, Hasmatuchi V, Münch-Alligné C, Franca MJ, Schleiss AJ, Ramos HM. Experimental characterization of a five blade tubular propeller turbine for pipe inline installation. Renew Energy 2016;95:356–66. https://doi.org/10.1016/j.renene.2016.04.023.

[12] Biner D, Hasmatuchi V, Avellan F, Munch-Alligne C. Design & performance of a hydraulic micro-turbine with counter-rotating runners. In: 2015 5th International Youth Conference on Energy (IYCE); 2015. https://doi.org/10.1109/iyce.2015.7180737.

[13] Vagnoni E, Andolfatto L, Richard S, Münch-Alligné C, Avellan F. Hydraulic performance evaluation of a micro-turbine with counter rotating runners by experimental investigation and numerical simulation. Renew Energy 2018;126:943–53. https://doi.org/10.1016/j.renene.2018.04.015.

[14] Jiyun D, Hongxing Y, Zhicheng S, Xiaodong G. Development of an inline vertical cross-flow turbine for hydropower harvesting in urban water supply pipes. Renew Energy 2018;127:386–97. https://doi.org/10.1016/j.renene.2018.04.070.

[15] Du J, Shen Z, Yang H. Effects of different block designs on the performance of inline cross-flow turbines in urban water mains. Appl Energy 2018;228:97–107. https://doi.org/10.1016/j.apenergy.2018.06.079.

[16] Chen J, Yang H, Liu C, Lau C, Lo M. A novel vertical axis water turbine for power generation from water pipelines. Energy 2013;54:184–93. https://doi.org/10.1016/j.energy.2013.01.064.

[17] Chen J, Lu W, Hu Z, Lei Y, Yang M. Numerical studies on the performance of a drag-type vertical axis water turbine for water pipeline. J Renew Sustain Energy 2018;10:044503. https://doi.org/10.1063/1.5027551.

[18] Langroudi AT, Afifi FZ, Nobari AH, Najafi A. Modeling and numerical investigation on multi-objective design improvement of a novel cross-flow lift-based turbine for in-pipe hydro energy harvesting applications. Energy Convers Manage 2020;203:112233. https://doi.org/10.1016/j.enconman.2019.112233.

[19] Malavasi S, Rossi MMA, Ferrarese G. Greenvalve: Hydrodynamics and applications of the control valve for energy harvesting. Urban Water J 2016;15:200–9. https://doi.org/10.1080/1573062x.2016.1175483.

[20] Lewis RI. Turbomachinery performance analysis. London New York: Arnold Wiley; 1996.

[21] Dixon S. Fluid Mechanics and Thermodynamics of Turbomachinery. Saint Louis: Elsevier Science & Technology; 2013.

[22] Rey R, Noguera R, Bakir F. Pompes rotodynamiques Aérohydrodynamique des profils et aubages de pompes hélices, volume base documentaire: TIB173DUO., Editions T.I., 2013. URL: https://www.techniques-ingenieur.fr/base-documentaire/mecanique-th7/machines-hydrauliques-pompes-et-helices-42173210/pompes-rotodynamiques-bm4304/, fre.

[23] Rey R, Noguera R, Bakir F. Pompes rotodynamiques Dimensionnement et analyse des performances des pompes hélices, volume base documentaire: TIB173DUO., Editions T.I., 2013. URL: https://www.techniques-ingenieur.fr/base-documentaire/mecanique-th7/machines-hydrauliques-pompes-et-helices-42173210/pompes-rotodynamiques-bm4305/, fre.

[24] Mataix C, Alonso A. Turbomáquinas hidráulicas: Turbinas hidráulicas, bombas, ventiladores. Biblioteca Comillas: Ingeniería, Universidad Pontificia Comillas (Publicaciones); 2009.

[25] Herrig L, Emery C, Erwin R. Systematic two dimensional cascade tests of NACA 65 – Series compressor blades at low speeds, Technical Report 3916, NACA; 1957.

[26] Weinig FS. General treatment of incompressible inviscid two-dimensional cascade flow. In Aerodynamics of Turbines and Compressors. (HSA-1). Vol. 1: Princeton University Press; 2017.

[27] Weinel E. Beiträge zur rationellen Hydrodynamik der Gitterströmung. Ingenieur-Archiv 1934;5:91–105. https://doi.org/10.1007/BF02086126.
[28] Shigemitsu T, Takeshima Y, Ogawa Y, Fukutomi J. Internal flow of contra-rotating small hydroturbine at off- design flow rates. IOP Conf Ser: Earth Environ Sci 2016; 49:102008. https://doi.org/10.1088/1755-1315/49/10/102008.
[29] Shigemitsu T, Ikebuchi T, Nan D, Hosotani T. Performance improvement of contra-rotating small hydroturbine. In: Renewable Energy and Sustainable Buildings. Springer International Publishing; 2019. p. 313–25. https://doi.org/10.1007/978-3-030-18488-9_24.
[30] Russo F, Basse NT. Scaling of turbulence intensity for low-speed flow in smooth pipes. Flow Meas Instrum 2016;52:101–14. https://doi.org/10.1016/j.flowmeasinst.2016.09.012.
[31] Drela M. Xfoil: an analysis and design system for low reynolds number airfoils. Low Reynolds Number Aerodyn 1989:1–12. https://doi.org/10.1007/978-3-642-84010-4_1.
[32] Chernoray V. Prediction of laminar-turbulent transition on an airfoil at high level of free-stream turbulence. Prog Flight Phys – Vol. 7; 2015. doi: 10.1051/eucass/201507491.
[33] Roy CJ. Review of code and solution verification procedures for computational simulation. J Comput Phys 2005;205:131–56. https://doi.org/10.1016/j.jcp.2004.10.036.
[34] Roache PJ. Perspective: a method for uniform reporting of grid refinement studies. J Fluids Eng 1994;116:405–13. https://doi.org/10.1115/1.2910291.
[35] Aakti B, Amstutz O, Casartelli E, Romanelli G, Mangani L. On the performance of a high head francis turbine at design and off-design conditions. J Phys: Conf Ser 2015;579:012010. https://doi.org/10.1088/1742-6596/579/1/012010.
[36] D.G. for Research, I.E. Commission. Turning FAIR into reality:final report and action plan from the European Commission expert group on FAIR data. Publications Office; 2018. doi: 10.2777/54599.
[37] Vivas A, Viedma A. Literate code of a novel approach to dimensionless design of tailored in-pipe pico-hydraulic turbines; 2021. doi: 10.5281/zenodo.4732832.
[38] Vivas A, Kaiser AS. Discretization uncertainty and numerical validation of a pico-hydraulic counter rotating turbine; 2021. doi: 10.5281/zenodo.4730962.
[39] Vivas A. Numerical characterization of a in-pipe axial pico-hydraulic turbine using OpenFOAM; 2021. doi: 10.5281/zenodo.4762901.
[40] Oertel H. Prandtl's essentials of fluid mechanics. New York: Springer; 2004.